CHEMISTRY OF MATERIALS

pubs.acs.org/cm

Article

# How to Quantify Electrons in Plasmonic Colloidal Metal Oxide Nanocrystals

Sofia A. Shubert-Zuleta, Bharat Tandon, Benjamin J. Roman, Xing Yee Gan, and Delia J. Milliron*

Cite This: *Chem. Mater.* 2023, 35, 3880−3891

Read Online

ACCESS | Metrics & More | Article Recommendations | Supporting Information

**ABSTRACT:** Distinct from noble metal nanoparticles, doped metal oxide nanocrystals (NCs) exhibit localized surface plasmon resonance (LSPR) in the infrared region that can be tuned by changing the free electron concentration through both synthetic and postsynthetic doping. Redox reagents have commonly been used to postsynthetically modulate the LSPR, but to understand the relationship between the electron transfer processes and the resulting optical changes, it is imperative to quantify electrons in the NCs. Titration and LSPR peak fitting analysis are the most common methods used for quantifying electrons; however, a comparison between these methods has previously revealed discrepancies up to an order of magnitude without a clear explanation. Here, we apply these electron quantification techniques concurrently to Sn-doped $In_2O_3$ NCs with varying size, doping concentration, and extent of postsynthetic reduction. We find that oxidative titration consistently overestimates the number of electrons per NC, owing to the failure of the assumed stoichiometric equivalents between moles of oxidant added and moles of free electrons extracted from the NCs. The NC characteristics we examine strongly influence the driving force for the oxidation process, affecting the relative agreement between oxidative titration and LSPR fitting; the two methods more closely agree when the electron transfer driving force is larger. Overall, these analyses inform best practices for quantifying electrons in plasmonic semiconductor NCs and reveal how the accuracy is affected by NC characteristics.

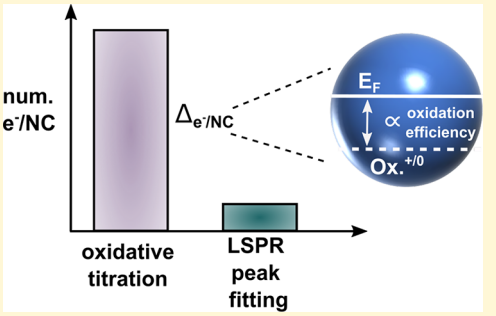




## INTRODUCTION

Doped metal oxide nanocrystals (NC) have recently attracted attention for their widely tunable localized surface plasmon resonance (LSPR), in which incoming light induces the collective oscillation of free carriers.[1−5] In noble metal NCs, LSPR tunability is mainly achievable via changes in morphology or size, while the LSPR in doped metal oxide NCs is readily tuned over a wide range by various doping strategies that alter the electron concentration, $n_e$, thus, inducing changes to the LSPR frequency according to the relation $\omega_{LSPR} \propto \sqrt{n_e}$.[5] Aliovalent doping, wherein charge-mismatched dopants are incorporated during NC synthesis, has been demonstrated for many colloidal metal oxide materials systems such as those based on $In_2O_3$,[6,7] ZnO,[8,9] CdO,[10] and furthermore, dopant segregation within the NC has proven to be useful for creating multimodal LSPR.[11−13] While aliovalent doping is useful for controlling the static LSPR of as-synthesized NCs, postsynthetic doping methods such as electrochemical doping,[14−18] photodoping,[9,19−22] and chemical doping[23−26] enable dynamic and reversible LSPR tunability. To understand how postsynthetic modulation of LSPR frequency, intensity, and line shape depends on the changing carrier concentration and to inform design of NCs for capacitive charge storage or optical modulation applications, it is critical to be able to reliably quantify the carriers in the NCs. Analysis is needed to determine the absolute number of carriers per NC and the carrier concentration (carriers per unit volume) as well as the differentials of these values during modulation.

Previous efforts in quantifying carriers in plasmonic NCs have largely relied on LSPR peak fitting with variations of the Drude model or oxidative titration of NC dispersions.[9,20−22,27−32] In the former, fitting the measured LSPR extinction peak according to Drude theory for a free electron gas, abbreviated as the simple Drude approximation (SDA), allows for estimation of the electron concentration from the LSPR peak frequency.[33] However, issues arise in SDA fitting because it conflates damping terms stemming from intrinsic damping and ensemble heterogeneity and neglects the effects of surface depletion on LSPR extinction and frequency. These oversights mean that electron quantification by the SDA possesses intrinsic inaccuracy for colloidal metal oxide NCs, typically overestimating due to the assumption that electrons

Received: December 13, 2022
Revised: April 3, 2023
Published: May 2, 2023

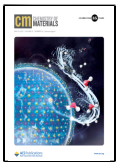

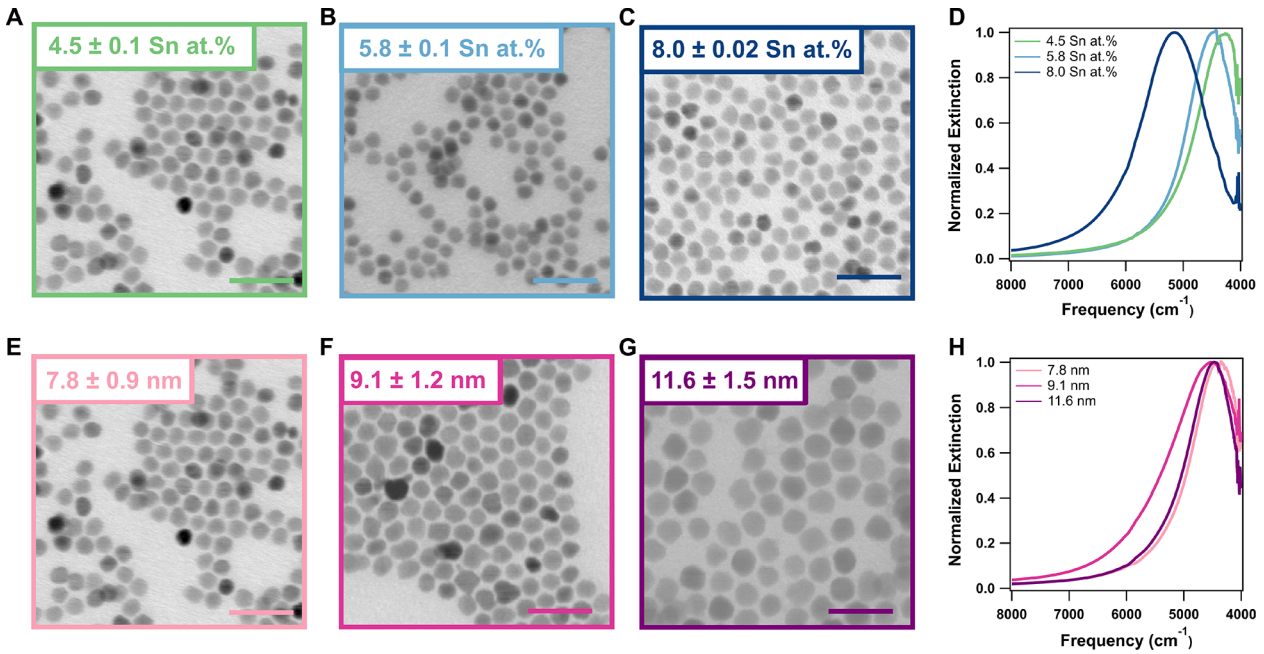


**Figure 1.** ITO nanocrystals synthesized for electron counting experiments. (A–C) STEM images and (D) normalized extinction spectra of doping series at 7.6 ± 0.4 nm, 4.5–8.0 Sn at. %. (E–G) STEM images and (H) normalized extinction spectra of size series at 4.5 Sn at. %, 7.8–11.6 nm. All extinction spectra are of ITO NCs dispersed in a 1:1 mixture of tetrahydrofuran and toluene. All scale bars in the STEM images are 30 nm.

occupy the entire NC volume, while in reality an electron-deficient surface depletion layer may occupy a substantial and variable portion of the NC volume.[15,21,34] Therefore, the Heterogeneous Ensemble Drude Approximation (HEDA) was developed to explicitly incorporate the effects of heterogeneity among the NC ensemble and surface depletion layers by considering experimentally measured values for size and NC concentration as fixed parameters to constrain the LSPR fit and, thus, correct for the overestimation of electrons per NC by the SDA.[35] The HEDA model has previously been used for electron quantification in both as-synthesized and postsynthetically reduced NCs; for example, electron transfer has been tracked from electroactive bacteria[36] and as a function of chemical reduction.[25]

Alternatively, titrating the NC dispersion with an oxidizing agent and tracking the decrease in LSPR extinction as a function of oxidation uses the extinction coefficient per free electron to extrapolate the total number of free electrons per NC.[32,37,38] Importantly, oxidative titration presumes that for each equivalent of oxidizing agent added, a free electron is extracted from a NC, hence diminishing the LSPR extinction. A key benefit of oxidative titration that distinguishes it from LSPR peak fitting is that quantification is equally possible when the LSPR peak maximum is outside the spectral window. Further, because oxidative titration is a model-independent method, it theoretically circumvents the inherent assumptions made by any particular fitting model. Despite LSPR peak fitting and oxidative titration being commonly used electron quantification techniques, comparison between the techniques has been limited in the literature and some examples published have reported large discrepancies between the methods.[20,27,28,30,39]

Most notably, one study compared fitting the LSPR peak using the SDA to oxidative titration with $NOBF_4$ on ∼10 nm diameter M:ZnO (M = $In^{3+}$, $Ga^{3+}$, $Al^{3+}$) NCs.[27] Electron concentrations calculated by oxidative titration were approximately 10 times higher than those calculated from fitting by the SDA, with the disagreement ascribed partially to reaction of $NOBF_4$ with pinned carriers, which reduces its efficiency as a titrating agent for free electrons. Quantification performed by oxidative titration indicated more than one free electron per dopant, with that ratio (known as activation) being as high as 1.91 in In-doped ZnO NCs. Activation exceeding 1.0 is unphysical, suggesting inflation of the oxidative titration quantification of free electrons. Similar experiments on ∼5 nm, 2.0–7.3 Sn at.% $In_2O_3$ revealed up to 2× larger electron concentrations found by $NOBF_4$ oxidative titration than with SDA fitting,[28] with the difference being attributed to failure of Drude theory incorrectly assuming a constant electron effective mass, $m^*$, and thus necessitating a correction factor be added to the Drude analysis. Further, a study on as-synthesized and surface passivated $WO_{3-x}$ nanoplatelets again revealed that $NOBF_4$ titration resulted in electron concentrations 1.5–2 times larger than those determined by LSPR peak fitting with the SDA.[30] Notably, $WO_{3-x}$ nanoplatelets that were capped with X-type alkylphosphonate ligands, meant to passivate surface trap states, displayed less discrepancy between the quantification methods than the as-synthesized nanoplatelets capped with carboxylate binding aliphatic ligands, suggesting that trap states in as-synthesized NCs may be a factor in the high electron quantification values often reported from oxidative titration analysis. Despite these disagreements between quantification methods reported throughout the literature, there has yet to be a systematic study of the factors impacting the discrepancies.

In this work, we explore the parameters that impact the agreement in quantification values between oxidative titration and LSPR peak fitting in degenerately doped metal oxide NCs. Specifically, Sn-doped $In_2O_3$ (ITO) NCs are used as a model plasmonic system for the excellent synthetic tunability of parameters such as size and Sn doping,[40] as well as the established capability for postsynthetic chemical doping.[19,20,25]


https://doi.org/10.1021/acs.chemmater.2c03694
Chem. Mater. 2023, 35, 3880–3891

By comparing electron quantification metrics calculated from LSPR peak fitting and oxidative titration in a single sample, we determine that oxidative titration leads to over 1.0 dopant activation values, which is unrealistic for $Sn^{4+}$ doped into $In_2O_3$ and suggests overestimation of electron quantification by oxidative titration. Further, we probe the factors that impact agreement between the quantification techniques by individually altering the extent of postsynthetic reduction, as-synthesized Sn doping concentration, and NC diameter. Especially in the case of titrating as-synthesized NCs, we observe oxidative titration overestimating the absolute number of electrons per NC and electron concentrations compared to those calculated by LSPR peak fitting, leading to the realization that the general assumption of initial quantitative extraction of electrons by oxidative titration is often violated, likely owing to oxidizing agents undergoing side reactions and thus performing inefficiently. We find that higher energetic driving force for oxidation leads to the oxidative titration values to be in better agreement with values obtained from LSPR peak fitting, which we attribute to the oxidation proceeding more efficiently and, thus, closer to the quantitative assumption. Overall, we conclude that the quantification methods agree the best for small NCs that have been substantially reduced prior to oxidative titration. The concurrent use of LSPR peak fitting and the canonical oxidative titration method in this study sheds light on the importance of considering electronic structure when quantifying electrons for dynamic LSPR tunability purposes.

## RESULTS AND DISCUSSION

The electronic structure of metal oxide NCs is dependent on synthetically controllable parameters such as the NC diameter and incorporated dopant concentration. To study the effects of such parameters on electron quantification discrepancy, spherical and monodisperse oleate-capped ITO NCs were synthesized via a slow-injection synthesis reported by Hutchison et al.[40] First, a series of NCs with near-constant size but varied Sn doping concentration was synthesized by varying the ratio of Sn to In in the precursor solution. Dopant incorporation in the resulting NCs ranged from 4.5 to 8.0 Sn at. % as determined by inductively coupled plasma-optical emission spectroscopy (ICP-OES) for a consistent NC diameter (7.6 ± 0.4 nm) and spherical morphology, as observed by scanning transmission electron miscroscopy (STEM) (Figure 1A-C). The LSPR frequency, $\omega_{LSPR}$, increases with Sn concentration, indicative of a higher free electron concentration (Figure 1D). The effect of NC diameter was studied by first synthesizing a series of NCs with different diameters, 7.8−11.6 nm, and approximately constant 4.5 ± 0.3 Sn at. % via similar synthetic methods (Figure 1E-H, Figure S1). The diameter was synthetically increased by injecting a larger volume of metal precursor solution into oleyl alcohol. While the $\omega_{LSPR}$ is expected to change modestly with increasing NC diameter due to a higher dopant activation and reduced surface scattering,[41] these effects are obscured by minor sample to sample variation in dopant concentration within the series. As will be further discussed, variation of the Sn doping concentration and size of ITO NCs results in distinct changes in the electronic structure; therefore, we use these size and doping series to further probe the impacts of electronic structure on the integrity of the electron quantification methods outlined previously.

Throughout this study, electron quantification methods based on LSPR fitting and oxidative titration were directly compared for each sample, as shown for a 7.8 nm, 4.5 Sn at. % ITO sample in Figure 2. Oxidative titration was performed in

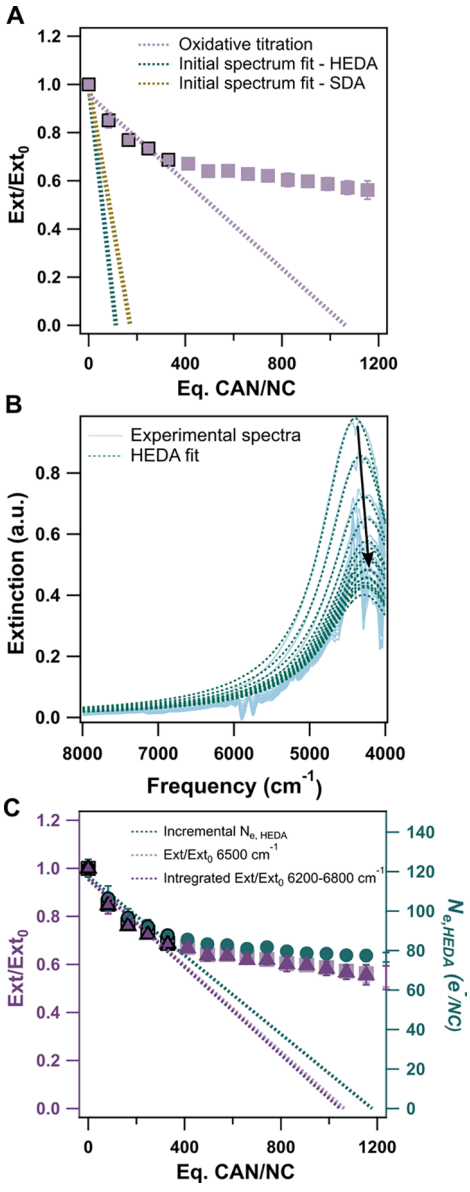


**Figure 2.** Example of oxidative titration on 4.5 Sn at. %, 7.8 nm ITO NCs. (A) Change in $Ext/Ext_0$ as a function of equivalents of CAN added per NC. Purple markers are experimental $Ext/Ext_0$, and those with black outline are considered the linear region. The line fit to this region corresponds to the slope determined by oxidative titration, while those derived by fitting the initial spectrum with the HEDA (teal line) and SDA (yellow line) models are theoretically determined based on the calculated $N_{init}$. (B) Experimental extinction (blue) and associated HEDA fits (dotted green) throughout the oxidative titration. (C) Comparison of different quantification methods that rely on extrapolation of the linear region. Oxidative titration methods correspond to the left, purple axis $Ext/Ext_0$. Extrapolating the linear portion of $Ext/Ext_0$ at a single frequency (6500 $cm^{-1}$, light purple squares) versus an integrated region (6200−6800 $cm^{-1}$, dark purple triangles) produces the same $N_{init}$. HEDA fitting the LSPR after each CAN addition tracks the change in the number of electrons ($N_{e,HEDA}$, teal circles) at each point of the titration and corresponds to the right teal axis.


https://doi.org/10.1021/acs.chemmater.2c03694
Chem. Mater. 2023, 35, 3880−3891

an inert atmosphere on as-synthesized NCs dispersed in a 1:1 mixture of tetrahydrofuran (THF) and toluene. Cerium ammonium nitrate (CAN) dissolved in acetonitrile (1.61 V vs NHE[42]) was chosen as the oxidizing agent for as-synthesized NCs because it has an oxidizing potential strong enough to extract Sn-compensated electrons, which are known to be very stable and difficult to oxidize.[9,19] Further, CAN is not known to significantly impact the oleate ligand shell of the ITO NCs, unlike $NOBF_4$, which is also commonly used as a ligand stripping reagent.[43,44] Following additions of CAN to the NC dispersion, *in situ* extinction spectra recorded showed a progressive red-shift and decrease in extinction of the LSPR (Figure S2), consistent with extraction of conduction band electrons. After several additions of CAN solution, a saturation point is reached beyond which additional CAN did not cause further red-shifting of the LSPR, indicating a limit to the oxidation had been reached, most likely due to a thermodynamic equilibrium being established between the CAN redox potential and the NC Fermi level, $E_F$.[32,38]

In keeping with the canonical method for quantifying electrons from oxidative titration, the extinction at a point in the tail of the LSPR (6500 $cm^{-1}$) relative to the extinction at the same frequency in the as-synthesized NCs, $Ext/Ext_0$, is tracked as a function of the number of equivalents of CAN added per NC (Figure 2A, purple markers). The resulting function can be split into 2 regions, the first being where $Ext/Ext_0$ decreases linearly with CAN additions (black outlined markers) and the latter being a plateaued region where the CAN oxidizing efficiency is greatly reduced and, thus, less effective at extracting free electrons. Making the commonly held assumption that CAN quantitively oxidizes the NC initially,[31,32] a line is fit to this region and extrapolated to the $x$-axis, where $Ext/Ext_0 = 0$. Theoretically, this intercept is the point at which all electrons would be extracted from the NC if the stoichiometric oxidation proceeded to completion, thus calculating the initial number of electrons per NC, $N_{init}$. To convert this value to the electron concentration of the initial NC dispersion before titration, $n_{init}$, $N_{init}$ was divided by the total NC volume. While using the total NC volume is expected to introduce error because it neglects surface depletion effects, we chose to do this to be consistent with previous reports that used oxidative titration to quantify $n_{init}$. This quantification method was performed in triplicate to confirm reproducibility and provide uncertainties associated with experimental variations (Figure S2).

Alternatively, the experimental extinction spectra obtained from the oxidative titration were fit by the HEDA model to extract the optoelectronic parameters governing the optical response (Figure 2B). The dielectric function of ITO is well-described by the Drude free electron model and fitting the LSPR to the idealized line shape predicted by Mie theory and neglecting depletion (i.e., SDA) allows for extraction of the electron concentration, $n_e$, as a fitting parameter.[33] Improving on this approach, fitting the experimental extinction spectrum to the HEDA model extracts additional information about the electronic properties of the NC ensemble but avoids over parametrization by incorporating additional experimentally determined information as fixed input parameters. Specifically, the mean and standard deviation of the NC radius and the volume fraction of NCs in the dispersion are measured independently by STEM and ICP-OES respectively and used to inform the fit. Fitting the experimental LSPR spectrum then results in the following optoelectronic parameters extracted: mean electron concentration ($n_e$), standard deviation in electron concentration ($\sigma_{n_e}$), electron accessible volume fraction ($f_e$), and bulk mean free path ($l_{bulk}$). Thus, fitting LSPR spectra to the HEDA model provides rich information quantifying electron transfer events *in situ*, revealing not only the number of electrons transferred but also their spatial distribution within the plasmonic metal oxide NCs.[25] Details regarding the SDA and HEDA models are included in the Supporting Information. Throughout this study, we report electron quantification from both HEDA and SDA fitting procedures; however, the values obtained from the HEDA model will be the focus of discussion because it is known to be more accurate than SDA fitting by accounting for surface depletion. It is important to note that the fits conducted with the SDA and HEDA models here all assume a constant conduction band electron effective mass, $m^*$, which is in line with previous reports showing that $m^*$ does not change significantly within the range of doping concentrations used in this work.[45]

$N_{init}$ calculated from HEDA fitting was performed by simply fitting the LSPR peak of the NCs prior to titration, which are as-synthesized NCs for the example in Figure 2. In contrast to oxidative titration or SDA fitting, we are able to account for the depletion layer in the HEDA fitting determined $N_{init}$ by scaling the NC volume by the electron accessible volume fraction output by the HEDA fitting ($N_{init} = n_{init}*(V_{NC}*f_e)$). The depletion layer considering $N_{init}$ from the HEDA fitting will be reported throughout this study. Comparing $N_{init}$ obtained from oxidative titration and HEDA fitting the LSPR peak revealed a 10× discrepancy between the quantification techniques (Table 1), with oxidative titration resulting in the larger $N_{init}$, similar to previous reports.[27,28,30]

**Table 1. Electron Quantification Values for the Sample Shown in Figure 2**

| Quantification Method | $N_{init}$ | $n_{init}$ ($10^{20}$ $cm^{-3}$) |
|---|---|---|
| Oxidative Titration | 1131 ± 210 | 46.5 ± 8.6 |
| Initial Spectrum Fit - HEDA | 113 ± 10 | 7.9 ± 0.12 |
| Initial Spectrum Fit - SDA | 170 ± 2 | 7.0 ± 0.07 |

To investigate the origin of this discrepancy, we first assessed the validity of monitoring $Ext/Ext_0$ at a single frequency throughout the titration rather than an integrated region, which effectively averages over many frequencies and better accounts for changes in the LSPR peak shape throughout titration (Figure 2C). Similar to the $Ext/Ext_0$ analysis performed at a single frequency (light purple), we plotted the $Ext/Ext_0$ integrated over 6200−6800 $cm^{-1}$ (dark purple) in the tail of the LSPR, then extrapolated the linear portion of the integrated $Ext/Ext_0$ to the $x$-axis to calculate $N_{init}$. The integrated and single frequency $Ext/Ext_0$ values were in good agreement and ultimately yielded the same $N_{init}$. Hence, $Ext/Ext_0$ at a single frequency will be reported throughout this work to be consistent with other reported methods and because it is most useful in cases where the entire LSPR signal is not within the spectral window. Next, we evaluated the legitimacy of the HEDA model when applied at each incremental CAN addition, analogous to the way $Ext/Ext_0$ is tracked throughout oxidation. The number of electrons per NC calculated from the HEDA fitting of each successive extinction spectra measured throughout the titration ($N_{e,HEDA}$)


https://doi.org/10.1021/acs.chemmater.2c03694
Chem. Mater. 2023, 35, 3880−3891

was used in place of $Ext/Ext_0$ from the oxidative titration quantification method (teal markers, right axis). Then, we apply the assumption of quantitative oxidation to the incremental $N_{e,HEDA}$ by fitting the initial linear region and extrapolating to the $x$-axis (equivalents of CAN per NC) to calculate $N_{init}$. This quantification method, termed incremental $N_{e,HEDA}$, and the experimental $Ext/Ext_0$ align closely throughout the oxidation process when overlaid, despite the different axes. The incremental $N_{e,HEDA}$ method consistently produces $N_{init}$ values approximately 15% larger than those obtained by tracking $Ext/Ext_0$, potentially as a result of the HEDA model's approximation of the radial electron concentration as a simplified core−shell geometry.[21,46] Electron quantification methods that rely on extrapolation of the linear region at the beginning of the titration must assume initial stoichiometric oxidation to calculate $N_{init}$. The fact that quantification methods that extrapolate the linear region all overestimate the electron concentration by approximately the same degree suggests that the stoichiometric oxidation assumption is in error (Figure 2C).

Importantly, regardless of the specific approach to quantifying the incremental spectral changes, oxidative titration results in higher $N_{init}$ values by approximately 1 order of magnitude in comparison to methods that fit the initial LSPR in accordance with the Drude model (Table 1), echoing a previous report on ITO NCs.[28] Converting the $N_{init}$ determined via titration to dopant activation translates to more than three free electrons generated per Sn dopant; this is unrealistic for aliovalent $Sn^{4+}$ when the host cation is $In^{3+}$ because the theoretical limit to achieve charge balance is one free electron compensated by one $Sn^{4+}$ dopant, and other compensating defects like oxygen vacancies are expected to be present only at low levels compared to substitutional Sn donors.[7] Conversely, LSPR peak fitting methods indicate a dopant activation of 0.33−0.5 electrons per Sn dopant, which is in line with the previously reported dopant activation of ITO NCs.[4,6,47,48]

This dopant activation analysis suggests that the spectral fitting results may be more accurate and calls into question the assumption of quantitative extraction of electrons within the linear region of oxidative titration. Reaction of CAN with $In_2O_3$ NCs, which we approximate as having no free electrons, resulted in a lower amount of CAN absorption than would be expected if CAN were added to the NCs and no NC oxidation were taking place, confirming that side reactions are indeed occurring (Figure S3). We hypothesize that the reaction of CAN with trapped electrons in surface states is likely a dominant source of the nonquantitative nature of the oxidation of free electrons;[28,30] however, other side CAN reactions may also contribute. Within this framework, the oxidation efficiency can be visualized by comparing the experimental change in $Ext/Ext_0$ throughout the titration (Figure 2A, purple line) with a theoretical slope derived from the LSPR peak fitting methods. For example, by setting the $Ext/Ext_0$ at 1.0 prior to any CAN addition, we assign the x-intercept as the $N_{init}$ calculated by LSPR peak fitting of the as-synthesized NCs. The resulting slope is a representation of how $Ext/Ext_0$ would change if CAN were to react stiochiometrically with free electrons, avoiding any other optically "silent" reactions. Here, either SDA or HEDA fitting results can be used, where the $N_{init,SDA}$ (yellow line) exceeds $N_{init,HEDA}$ (teal line) because SDA fitting assumes the derived electron concentration is constant throughout the NC volume, whereas the HEDA model fits for the electron accessible volume fraction, thus limiting the calculated $n_{init,HEDA}$ to a smaller occupied volume. In the case of fitting with the HEDA model, $N_{init}$ is found by multiplying the electron concentration found by fitting by the plasmonic volume. For this reason, $N_{init}$ calculated by HEDA fitting will be used when comparing oxidative titration to the LSPR peak fitting. Having observed the ∼10x discrepancy in $N_{init}$ between oxidative titration and LSPR fitting, we sought to understand the factors influencing the quantitative disagreement by varying the characteristics of the NCs and their initial charge state.

**Effect of Chemical Reduction.** Oxidative titration has commonly been performed on postsynthetically reduced NCs[19−21,37,49] to quantify the preceding reduction of the NCs by either photoexcitation and hole scavenging (i.e., photodoping) or by a chemical reducing agent. There is still much to be understood about the diverse effects on band structure and surface chemistry by postsynthetic doping and subsequent oxidation. In the case of chemically induced redox reactions on NCs, the precise charging mechanism and its impacts on the NC surface are not yet well understood. It is possible that the $Sn^{II}/Sn^{IV}$ or the O vacancy concentration could be changing, or alternatively, the surface could remain chemically the same, but an electrical double layer is formed where ions are collected to compensate for the change in electron concentration in the NC. Regardless of the charge storage/extraction mechanism, we do not expect this to significantly impact electron quantification accuracy. Rather, postsynthetic reduction is known to raise the NC Fermi level and narrow the depletion layer width,[19,25] but the implications of these changes on electron quantification methods are currently unknown.

To investigate how the extent of reduction impacts the agreement between electron quantification methods, we compared ITO NCs that had been reduced to a variable extent with decamethyl cobaltocene ($CoCp_2^*$) before undergoing oxidative titration.[25,38] $CoCp_2^*$ is a strong reducing agent that is frequently used with metal oxide NCs and donates electrons via proton-coupled electron transfer (PCET) in the presence of a proton source.[50] A reduction series was prepared using a single batch of 7.8 nm, 4.5 Sn at. % ITO NCs that was divided into three dispersions to minimize sample variations. To each dispersion, 25 $\mu$L of 0.02 M $[(OEt_2)_2H]^+[BAr_4^F]^-$, otherwise known as Brookhart's acid, was added to facilitate the PCET reduction. Next, a 5 $\mu$L addition of $CoCp_2^*$ at varying concentration was added, and the extinction spectrum was recorded after this reduction. An increased $CoCp_2^*$ concentration led to an increased blue-shift in the $\omega_{LSPR}$, indicative of electron transfer to the NCs according to Drude theory.

Reducing the three dispersions with increasing concentration of 5 $\mu$L $CoCp_2^*$ from ∼0.004−0.02 M led to blue-shifts of $\Delta\omega_{LSPR}$ = 249 $cm^{-1}$, 342 $cm^{-1}$, and 591 $cm^{-1}$ (Figure S4). Oxidative titration was then carried out with $[FeCp_2^*]^+$, which was chosen over CAN because oxidation with CAN after the addition of Brookhart's acid and $CoCp_2^*$ led to precipitation of the NCs, whereas $[FeCp_2^*]^+$ retained colloidal stability throughout the oxidative titration. Further, we observed in each of the three reduction cases that the first two additions of $[FeCp_2^*]^+$ seemed ineffective at oxidizing the NCs, evidenced by little change in the LSPR peak and the $Ext/Ext_0$ in the tail of the LSPR. We attributed this to $[FeCp_2^*]^+$ initially reacting with excess Brookhart's acid in solution rather than oxidizing


https://doi.org/10.1021/acs.chemmater.2c03694
Chem. Mater. 2023, 35, 3880−3891

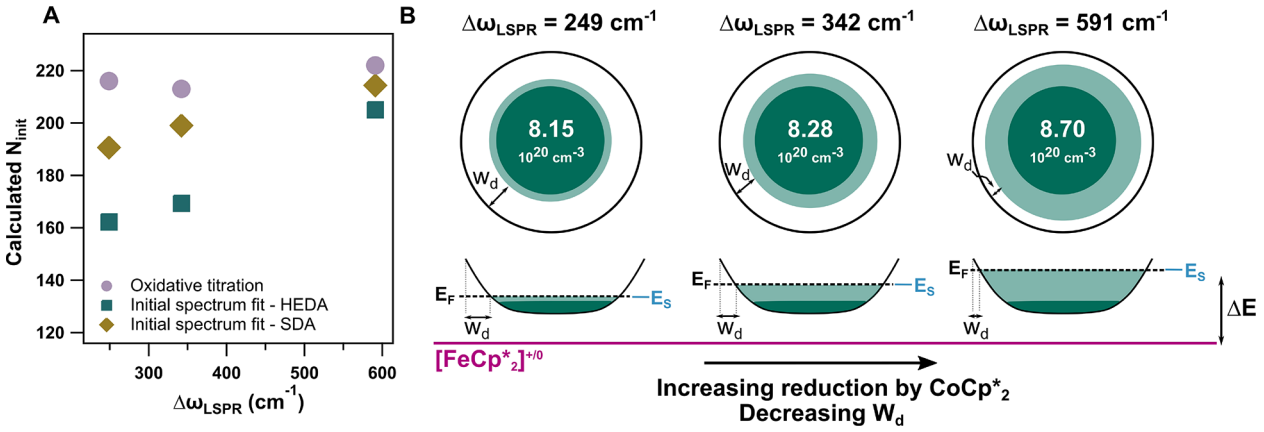


**Figure 3.** (A) Calculated $N_{init}$ for 7.8 nm, 4.5 at. % Sn ITO at various stages of reduction by $CoCp^*_2$. Higher $\omega_{LSPR}$ values are indicative of further reduction. $[FeCp^*_2]^+$ was used for the oxidative titration method because it preserved the colloidal stability of the NCs. (B) Schematic of the change in the radial conduction band profile with increasing $CoCp^*_2$ reduction. $E_S$ denotes surface potential at which $E_F$, the Fermi level, is pinned. $\Delta E$ indicates the potential difference between $E_F$ and the redox potential of the oxidizing agent. Shading represents conduction band electron concentration from aliovalent doping (dark green) and postsynthetic doping (light green). Values inside the NC schematics are the $n_{init}$ values determined by HEDA fitting the LSPR of the reduced NCs.

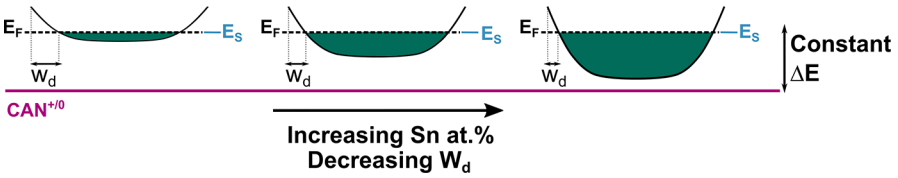


**Figure 4.** Effect of Sn doping concentration on the as-synthesized ITO radial band structure. $E_S$ denotes the surface potential.

NC electrons. Decreasing the amount of acid added to counteract this effect would conversely result in insufficient protons for the $CoCp^*_2$ to fully react and would leave excess $CoCp^*_2$ in the NC dispersion, which would lead to a plateau region similar to that in the case of excess acid. Rather than attempting to precisely balance the amounts of acid and $CoCp^*_2$ in solution, we chose to add a constant amount of Brookhart's acid (25 $\mu$L) across the reduction series and shift the $Ext/Ext_0$ curves from oxidative titration to eliminate the initial plateau region caused by the excess acid. Compared to an instance where the amounts of acid and $CoCp^*_2$ added were balanced nearly perfectly and there was no plateau region, the electron quantification values were in good agreement (Figure S5). We found that decreasing the equivalents of $[FeCp^*_2]^+$/NC per titration addition revealed a slightly steeper slope of $Ext/Ext_0$ at low amounts of $[FeCp^*_2]^+$ added compared to intermediate amounts before the full plateau region had been reached (Figure S6). Hence, limiting the fit to a linear region at low amounts of added oxidant, where the oxidation efficiency is likely to be maximized, can produce more accurate electron quantification values.

The number of electrons per NC *after reduction*, referred to again as $N_{init}$, was quantified via both the oxidative titration method and LSPR peak fitting of the extinction spectrum following $CoCp^*_2$ reduction (Figure 3a, Tables S1−S2). By fitting the LSPR peak, we found $N_{init}$ values for the reduced NCs that increased, as expected with the extent of reduction. Based on HEDA fitting, up to 92 electrons per NC were added by $CoCp^*_2$ in the most reduced case. Interestingly, $N_{init}$ calculated by oxidative titration with $[FeCp^*_2]^+$ was near constant, 217 ± 4 electrons per NC, regardless of the amount of $CoCp^*_2$ used to reduce the NCs, despite the spectral shifting that suggests a definite systematic variation in the electron populations. In plotting $Ext/Ext_0$ as a function of $[FeCp^*_2]^+$ equivalents added per NC (Figure S7), $Ext/Ext_0$ changes more rapidly within the initial linear region for the NCs that have been reduced further. Considering that the same amount of NCs is used for each reduction in this study, this steeper slope indicates higher selectivity of $[FeCp^*_2]^+$ at extracting conduction band electrons versus undergoing side reaction, thus causing the extinction to diminish faster and improving the overall oxidation efficiency. Similarly, the slope of $Ext/Ext_0$ throughout oxidative titration has previously been interpreted as oxidizing agent efficiency in InN NCs,[32] where stronger oxidizing agents led to more efficient extraction of free electrons and, thus, a steeper change in $Ext/Ext_0$.

Here, we rationalize the increase in oxidation efficiency with a greater extent of reduction based on the altered electronic structure as a consequence of the initial reduction (Figure 3B). LSPR fitting with the HEDA model reveals that as NCs are reduced by $CoCp^*_2$, $n_e$ in the core is increased while the depletion layer width, $W_d$, narrows, thus expanding the electron accessible volume (Figure S8). These changes are consistent with postsynthetic reduction raising the $E_F$ and increasing the conduction band filling.[15,20] Therefore, the correlation between oxidation efficiency and NC reduction could be attributed to two potential factors: 1) the narrowed $W_d$ increases the propensity for electron transfer across the depletion layer from the electron-rich core to the oxidizing agent at the NC surface; and 2) as the Fermi level is raised during the reduction process, the potential difference between electrons at the Fermi level and the redox potential of the oxidizing agent ($\Delta E$) is increased, thus resulting in a larger driving force for oxidation.

**Effect of Sn Doping.** To determine which of the possible factors, depletion layer width and driving force, most impact


https://doi.org/10.1021/acs.chemmater.2c03694
Chem. Mater. 2023, 35, 3880−3891

the oxidative efficiency, we performed comparative electron counting analyses on a series of ITO NCs with different Sn doping concentrations. Higher Sn dopant concentrations cause the valence and conduction bands to bend more steeply, hence, reducing $W_d$ without affecting $E_F$ or $\Delta E$ (Figure 4). Previous studies comparing aliovalent and postsynthetic doping have demonstrated that aliovalent doping has little impact on the Fermi level; rather, it lowers the conduction band edge, causing the bands to bend more.[9,19,20] In contrast, postsynthetic doping techniques maintain the overall conduction and valence band potentials while primarily shifting $E_F$.[9,19,20] The distinct impacts of aliovalent doping and postsynthetic doping on the Fermi level were proven by greater stabilization of $Sn^{4+}$ compensated electrons compared to postsynthetically added electrons. To study the case of narrowing $W_d$ at constant $\Delta E$, oxidative titration with CAN was performed in triplicate on a series of ITO NCs with diameter 7.6 ± 0.4 nm and variable dopant concentration of 4.5−8 Sn at. %, the samples shown in Figure 1A−D (Figure S9). Electron quantification using the aforementioned techniques revealed that the discrepancy in calculated $N_{init}$ between oxidative titration and HEDA fitting of the as-synthesized LSPR peak tends to be modestly larger as more Sn is incorporated in the NCs (Figure S10, Tables S3−S4). A related observation has previously been reported for doped ZnO NCs, where the disparity between SDA fitting and $NOBF_4$ titration determined $N_{init}$ values was increased in NCs with higher electron concentration from aliovalent trivalent dopants.[27]

Considering that trends in $N_{init}$ values can be distorted by even minor sample to sample variation in the doping concentration or size, they must be properly normalized to compare quantification metrics across a series. For example, the somewhat smaller size, 7.1 nm, of the 5.8 Sn at. % ITO NCs would naturally reduce the $N_{init}$ for this sample for reasons unrelated to the dopant-dependent accuracy of the quantification methods. Normalizing by NC volume gives $n_{init}$, which allows a more direct assessment of the trends and results in the expected monotonic increase with the Sn-doping concentration based on LSPR analysis (Figure 5A). To more directly expose the differences between the quantification methods, the electron count can be further normalized by the Sn concentration, yielding the apparent dopant activation (i.e., electrons counted per Sn present) for each sample. Practically speaking, dopant activation is found by dividing the respective $N_{init}$ values by the total number of Sn dopant atoms determined by ICP-OES analysis (Figure 5B). Dopant activations based on $N_{init}$ values from HEDA fitting were approximately 0.3 for all samples, which is in line with previously reported dopant activation for ITO NCs.[4,6,47,48] In contrast, oxidative titration consistently overestimated approximately 3.0 activation, or more than 3 electrons per $Sn^{4+}$, across the doping series. This unphysical result further confirms the nonquantitative nature of extracting electrons from as-synthesized ITO NCs using a chemical oxidizing agent; however, the near constancy of these dopant activation values suggests that oxidation efficiency is independent of Sn doping concentration. Considering that $\Delta E$ is also constant across the doping series while $W_d$ varies substantially, these findings point to $\Delta E$ being the dominant factor governing oxidation efficiency. While it is possible that $W_d$ does have a kinetic effect on electron oxidation, i.e., hindering the electron transfer rate, $\Delta E$ controls the propensity for extraction of free electrons over side reactions and, thus, oxidation efficiency.

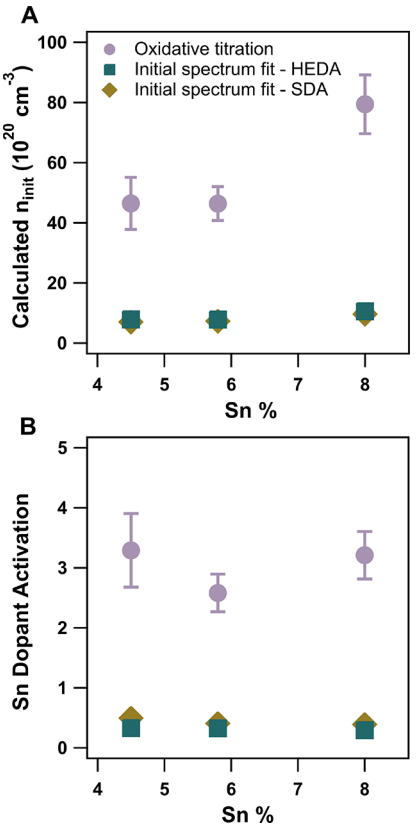


**Figure 5.** (A) Calculated electron concentration, $n_{init}$ and (B) corresponding Sn dopant activation for ITO NCs ranging from 4.5 to 8.0 Sn at. %, 7.6 ± 0.4 nm.

**Effect of NC Diameter.** Finally, we sought to systematically investigate the effect of the NC size on the agreement of the two electron quantification methods. In many studies using oxidative titration to quantify electrons, the NCs are small, less than 8 nm, and the disparity in electron quantification values between LSPR peak fitting and oxidative titration seems to be heightened for larger metal oxide NCs. For example, 5.0 ± 0.5 nm ITO NCs displayed up to 2× overestimation of the electron concentration by oxidative titration,[27] whereas the disagreement for 10 ± 0.3 nm M:ZnO (M = $Al^{3+}$, $Ga^{3+}$, $In^{3+}$) was up to 18×.[28] While there may be other factors at play that contribute to the discrepancies in the aforementioned examples (e.g., composition-dependent electronic structure), NC diameter seems to play a role that is yet to be understood. To elucidate the effect of size on LSPR peak fitting and oxidative titration as electron quantification methods, we synthesized a series of ITO NCs at 4.5 ± 0.3 Sn at. % ranging from 7.8 to 11.6 nm in diameter (Figure 1E-H). Similar to previous samples, each NC dispersion was oxidatively titrated with CAN in an anhydrous and inert environment (Figure S11). Comparing $N_{init}$ quantified by LSPR peak fitting and the oxidative titration methods (Figure 6A, Table S5−S6) revealed that the discrepancy rapidly increased for larger diameters. Most of the growing disparity is due to the magnification of error by the volume of each NC, with the volume-scaled $n_{init}$ having far less size dependence (Figure 6B). Quantified by oxidative titration, $n_{init}$ is several times higher than values determined by LSPR fitting and is near constant at the smaller


https://doi.org/10.1021/acs.chemmater.2c03694
Chem. Mater. 2023, 35, 3880−3891

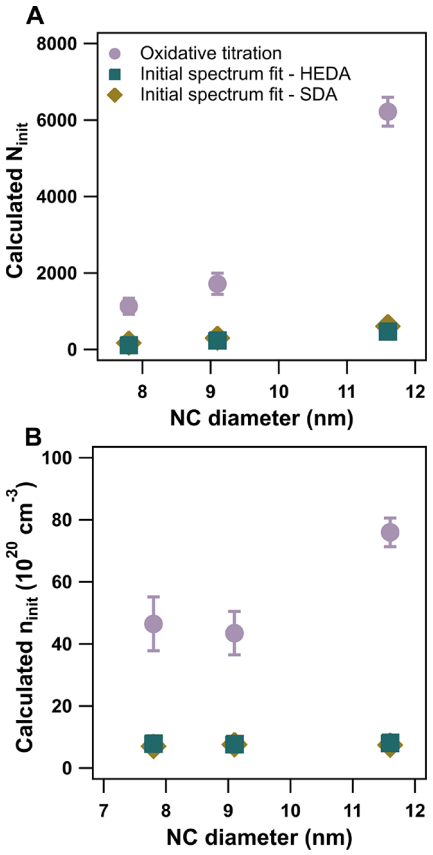


**Figure 6.** Calculated (A) $N_{init}$ and (B) $n_{init}$ for NCs ranging from 7.8 to 11.6 nm, all with 4.5 Sn at. % concentration.

NC diameters of 7.8 and 9.1 nm, increasing for the 11.6 nm NCs. Considering the connections between band structure and oxidation efficiency revealed by the reduction and doping series, we examined how the band structure might impact the oxidation efficiency at varying NC diameters. Similar to the case of Sn doping concentration, the initial $E_F$ is independent of NC diameter, being pinned at the surface in a manner dictated by surface states that are not expected to change their energies significantly within this NC size range (Figure S12).[15,35] Therefore, the initial oxidation efficiency is expected to be size-independent because the potential difference between $E_F$ and the redox potential of CAN ($\Delta E$) is the same across the as-synthesized samples. Constant $E_F$ across the NC diameters is confirmed by finding that $W_d$ derived by HEDA fitting is size-independent. For constant doping concentration, $W_d$ is approximately independent of size (curvature effects are limited in this size range), but does depend directly on $E_F$ and can be used as an indicator of the surface-pinned Fermi energy (Figure S13, eq S6). Size-independent oxidation efficiency implies oxidative titration should result in a near constant $n_{init}$ with size, yet our results indicate a further source of discrepancy between quantification methods that impacts larger NCs. To confirm this trend, we conducted the same quantification methods on a 21 nm, 4.5 Sn at. % NC dispersion and found that successive additions of CAN lead to exceedingly small decreases in extinction, thus, resulting in shallow $Ext/Ext_0$ throughout titration and overestimation of $n_{init}$ by over 80× compared to fitting the as-synthesized LSPR with the HEDA model (Figure S14). The greater overestimation of $N_{init}$ and $n_{init}$ by oxidative titration of larger NCs highlights that the small changes in LSPR extinction for larger diameter NCs magnify the error from all other factors that impact the LSPR extinction, making oxidative titration challenging and unreliable for electron quantification at larger NC sizes.

A potential strategy for improving the accuracy of oxidative titration for larger NCs is to initially reduce the NCs to enhance the oxidative efficiency. For example, a study wherein maximally photodoped 14 nm, 0−3.5 Sn at. % ITO NCs were oxidatively titrated resulted in more reasonable electron quantification values ranging from 190 to 535 electrons per as-synthesized NC,[19] values that are the same order of magnitude as those found by LSPR peak fitting. Initial reduction of these larger NCs highlights the key role that the driving force plays in oxidative titration proceeding efficiently, leading to more accurate electron quantification.

## CONCLUSIONS AND OUTLOOK

In conclusion, by studying oxidative titration and LSPR peak fitting concurrently, we have established that electron quantification by oxidative titration consistently overestimates $N_{init}$ in ITO NCs due to nonquantitative (i.e., inefficient) extraction of conduction band electrons. In the future, the exact nature of side reactions undergone by the oxidizing agent, leading to this inefficiency, should be studied more extensively, and possible strategies should be devised to circumvent these deleterious reaction pathways. As shown here for metal oxide NCs, the selectivity for oxidation of conduction band electrons can be maximized by establishing a large driving force via postsynthetic doping. It is advantageous to maximize the driving force by oxidizing high potential postsynthetically added electrons rather than simply using a stronger oxidizing agent, which can increase the probability of side reactions and hinder quantitative oxidation. Complementary studies on the effects of postsynthetic reduction and Sn doping concentration revealed that energetic difference between the Fermi level and redox potential of the oxidizing agent, $\Delta E$, controls the driving force for oxidation of conduction band electrons. Therefore, maximizing $\Delta E$ via postsynthetic reduction results in oxidation proceeding closer to the assumption of quantitative extraction of electrons, making oxidative titration more accurate. Additionally, while the oxidation efficiency is expected to be constant with NC diameter, larger NCs undergo very little relative change in overall electron concentration or population and, thus, optical response, per addition of oxidizing agent. This modest change in LSPR extinction throughout oxidation exacerbates any competing factors that might impact the LSPR and makes the oxidative titration of large as-synthesized NCs challenging and vulnerable to inaccuracy. Combining the results on the effects of postsynthetic reduction, aliovalent doping, and NC diameter reveal that while fitting with the HEDA model likely produces the most accurate and broadly applicable electron quantification method for ITO NCs, in scenarios where LSPR peak fitting is not possible, oxidative titration can be used if the NC electronic structure is considered to gauge the accuracy the quantification results. Given that similar overestimation by oxidative titration has been reported in other metal oxide NC systems, we expect that the observed trends will extend to a wider class of plasmonic doped metal oxide materials, albeit to different extents depending on their specific electronic band structures. Since HEDA analysis has so far been applied only to doped $In_2O_3$ NCs, these observations also motivate the further development


https://doi.org/10.1021/acs.chemmater.2c03694
Chem. Mater. 2023, 35, 3880−3891

of quantitative analysis methods for LSPR in other plasmonic doped oxide NC materials, e.g., ZnO, $WO_{3-x}$, and CdO. While this study focused on chemical reduction of the NCs, comparing the charging mechanisms and agreement in electron quantification methods for other postsynthetic doping techniques will shed light on the unique band structure changes that come with different doping processes. Broadly speaking, electron quantification is necessary for accurately assessing the charge storage properties of colloidal semiconductor NCs, which is vital for integrating these materials into sensing, catalytic, and optoelectronic applications.

## EXPERIMENTAL METHODS

**Chemicals.** The following chemicals used to synthesize ITO NCs were purchased commercially and were not further purified upon use: Indium(III) acetate (STREM, ≥ 99.99%), tin(IV) acetate (Sigma-Aldrich, ≥ 99.99%), oleyl alcohol (Sigma-Aldrich, ≥ 85%), and oleic acid (Sigma-Aldrich, ≥ 90%). Oleylamine (Sigma-Aldrich, ≥ 70%), ethanol (Fischer Chemical, ≥ 90%), hexane (Fischer Chemical, ≥ 99.9%), tetrahydrofuran (Sigma-Aldrich, ≥ 99.9%), and toluene (Sigma-Aldrich, ≥ 99.8%) were used to prepare the NC dispersion for reduction and oxidative titration. For reduction, sodium tetrakis[3,5-bis(trifluoromethyl)phenyl]borate and bis-(pentamethylcyclopentadienyl) cobalt(II) were purchased from Sigma-Aldrich and dried under vacuum at 100 °C for 16 h prior to use. For preparation of $[FeCp^*_2]^+[BAr_4F]^-$ oxidizing agent, Bis-(pentamethylcyclopentadienyl) iron(II) (Sigma-Aldrich, ≥ 97%), iron(III) chloride hexahydrate (Sigma-Aldrich, ≥ 97%), and sodium tetrakis[3,5-bis(trifluoromethyl)phenyl]borate were used as purchased. Cerium ammonium nitrate (Sigma-Aldrich, 98.5%) was purchased commercially and dried under vacuum at 100 °C for 16 h prior to use.

**Nanocrystal Synthesis.** ITO NCs were synthesized following a slow-injection method developed by Hutchison et al.[40] Briefly, $In(Ac)_3$ and $Sn(Acac)_4$ precursors were dissolved in oleic acid for a total metal concentration of 0.5 M, and the stoichiometric ratio of the precursors was adjusted for the desired doping concentration. The solution was stirred and degassed on a standard Schlenk line at 80 °C. The flask was then put under a $N_2$ flow and allowed to stir at 120 °C for 2 h. Using a 10 mL syringe and syringe pump, the precursor solution was then injected into a separate flask of oleyl alcohol at 290 °C at a flow rate of 0.2 mL/min under $N_2$ flow. Increasing the injection volume resulted in NCs with larger diameter but maintained the same Sn doping concentration. Following the injection, the flask was immediately taken off the heat, cooled to room temperature, and the NCs were precipitated with ethanol, centrifuged at 9000 rpm for 5 min, and the resulting NC pellet was redispersed in hexanes. The washing process was repeated 3 more times, adding oleic acid and oleylamine in volumes 1% of the total NC dispersion volume after the first washing procedure. After washing, the NC dispersion in hexane was filtered through a 0.2 μm PTFE filter.

**Characterization.** *Scanning Transmission Electron Microscopy (STEM).* ITO NC samples were prepared by drop-casting 10 μL of dilute NC dispersions on Cu 400-mesh TEM grids with carbon support films and drying the grids for several days in a vacuum desiccator. The samples were imaged on a Hitachi S5500 with an accelerating voltage of 30 kV and 10 mA beam current operating in bright field STEM mode. At least 1000 NCs per sample were analyzed using ImageJ software to determine the NC size.

*Inductively Coupled Plasma-Optical Emission Spectroscopy (ICP-OES).* Volume fractions and doping concentrations of the ITO NCs were determined by ICP-OES on a Varian 720-ES ICP optical emission spectrometer. Samples were prepared by drying a known volume of NC stock solution and digesting the resulting pellet in aqua regia for at least 72 h. The digested sample was diluted with Milli-Q water to a final concentration that was approximately 2% acid by volume. Standard solutions of increasing concentrations were prepared containing known amounts of In and Sn commercial ICP-OES standards and diluted with a 2% $HNO_3$/Milli-Q water. The Sn doping concentration was calculated by dividing the Sn concentration by the total In+Sn metal concentration determined by ICP-OES. The volume fraction was determined by first calculating the ITO concentration from In and Sn metal concentrations obtained by ICP-OES, and then converting to volume fraction using a density of 7.14 g/mL. Using the known volumes of the samples, the volume fractions of the dispersions used for chemical titration were calculated.

**Chemical Titrations.** *Oxidative Titration on As-Synthesized NCs.* As-synthesized ITO NCs were precipitated from the native hexane solvent with ethanol, redispersed in a tetrahydrofuran (THF)/toluene (1:1) mixture, and filtered with a 0.2 μm PTFE filter, in an anhydrous, Ar atmosphere. The NCs were diluted further with THF/toluene to achieve an initial optical density ranging from 0.5 to 1.0, all in a 1 mm path length quartz cuvette. Cerium ammonium nitrate (CAN) was used as the oxidizing agent to extract the very stable Sn-compensated conduction band electrons. After drying, the CAN concentration was calculated by dissolving a known mass of CAN in a known volume of acetonitrile. CAN was added to the NC dispersion at a 2.7 mM concentration through successive additions to carry out the titration. *In situ* extinction spectra were recorded after each addition using a fiber-coupled ASD Inc. PANanalytical spectrometer. Measurements were recorded 1.5 min after CAN addition, with the cuvette being vigorously shaken during the waiting time. Three replicates of titrations were performed for each sample to confirm the reproducibility. Eventually, large amounts of CAN (<10 additions) did cause NC aggregation; however, the decrease in LSPR frequency and extinction as a function of oxidation had always plateaued before this point. This suggests that after the thermodynamic limit on oxidation is reached, reaction with NC ligands becomes more prevalent, thus, destabilizing the NCs. To calculate $N_{init}$, the number of electrons in the as-synthesized NCs, the extinction at 6500 $cm^{-1}$ relative to that of the as-synthesized NCs ($Ext/Ext_0$) was plotted against the equivalents of CAN per NC. The only exception to this was the 8.0 Sn at. % sample in the doping series. Due to the blue-shift of the LSPR with increased Sn concentration, 6500 $cm^{-1}$ was not sufficiently in the tail of the LSPR. Rather, 9500 $cm^{-1}$ was at a comparable position in the LSPR tail as 6500 $cm^{-1}$ was for the 4.5 Sn at. % sample, and thus, 9500 $cm^{-1}$ was used to track the $Ext/Ext_0$ throughout oxidative titration for the 8 Sn at. % sample. A line was fit to the initial linear portion and extrapolated to the *x*-axis, where theoretically all electrons have been oxidized, thus determining $N_{init}$.

*Oxidative Titration on Reduced NCs.* The redox titrations were performed on a single batch of 7.8 nm, 4.5 Sn at. % NCs to avoid sample variations within the experiment, which were prepared as outlined above. Brookhart's acid, $[H(OEt_2)_2]^+[BAr^F_4]^-$, was prepared according to previous literature reports[51] and diluted to 0.02 M, with the solution containing 30% by volume equal parts oleylamine and oleic acid ligands. To the NC dispersion was added 25 μL of the ligand-stabilized 0.02 M acid solution was added. The NCs were then partially reduced by a 5 μL addition of $CoCp^*_2$ in THF. Reducing the NCs with increasing concentration of 5 μL $CoCp^*_2$, ranging from ~0.004−0.02 M, resulted in blue-shifts of $\Delta\omega_{LSPR}$ = 249 $cm^{-1}$, 342 $cm^{-1}$, and 591 $cm^{-1}$. Following, oxidative titration was carried out with $[FeCp^*_2]^+$ instead of CAN because adding CAN to chemically reduced NCs led to near immediate NC aggregation, potentially due to reaction with side products of the reduction process. $[FeCp^*_2]^+[BAr^F_4]^-$ was prepared according to previous literature reports[52] and dissolved in a 1:1 THF and toluene mixture at 0.8 mM. Following the reduction, 5 μL of this solution was added to the cuvette 15 times at 1.5 min intervals, with spectra recorded between each addition as outlined above. As previously described, excess Brookhart's acid in solution initially reacted with $[FeCp^*_2]^+$, leading to no change in $Ext/Ext_0$ for the first two additions, $[FeCp^*_2]^+$. Therefore, the $Ext/Ext_0$ curves for all samples in the reduction series were shifted to eliminate this initial plateau region. $N_{init}$, which in this case was the number of electrons per reduced NC, was determined by plotting $Ext/Ext_0$ at 8000 $cm^{-1}$ (to account for the blue-shift of the LSPR) against the equivalents of $[FeCp^*_2]^+$ added per NC and extrapolating the fit of the linear region to the *x*-axis.


https://doi.org/10.1021/acs.chemmater.2c03694
Chem. Mater. 2023, 35, 3880−3891

**LSPR Peak Fittings.** An in-depth discussion on the development of and theory behind the HEDA model and the associated MATLAB code can be found in ref.[35] Briefly, the HEDA model takes in the experimental extinction spectrum and three experimentally determined input parameters, the mean and standard deviation of the NC radius and the NC volume fraction, $f_v$. The radius parameters were obtained by analysis of STEM images and the NC volume fraction was determined by ICP-OES. The model then fits the LSPR peak for four terms, the carrier concentration ($n_e$), standard deviation in the carrier concentration ($\sigma_{n_e}$), mean free path, $l_{mfp}$, and electron accessible volume fraction, $f_e$, and outputs the fitted extinction spectrum. Building upon the Drude approximation, the HEDA model accounts for heterogeneity in the NC dispersion, both size and electron concentration heterogeneity. The model also accounts for the near-surface depletion region reported for many metal oxide NC species[34] by fitting for $f_e$, the volume fraction of the plasmonic core where electrons reside. Finally, surface scattering is considered in the calculation of $l_{mfp}$ using $l_{bulk}$ as a fitting parameter.

Boundaries were placed on $l_{mfp}$ to ensure the realistic fit results. An upper bound of 17 nm is placed on $l_{mfp}$ in accordance with experimentally determined values for $l_{bulk}$ in bulk ITO.[53] For NCs smaller than $l_{bulk}$, surface damping is the dominant damping mechanism, and considering that most of the ITO NCs used in this work are 7−12 nm in diameter, it is the dominant factor contributing to overall damping and to $l_{mfp}$.

## ■ ASSOCIATED CONTENT

### Supporting Information

The Supporting Information is available free of charge at https://pubs.acs.org/doi/10.1021/acs.chemmater.2c03694.

Further data regarding the extinction throughout titrations, electron quantification comparisons, additional band structure diagrams and tabulated data (PDF)

## ■ AUTHOR INFORMATION


### Corresponding Author

**Delia J. Milliron** − *McKetta Department of Chemical Engineering, University of Texas at Austin, Austin, Texas 78712, United States; Department of Chemistry, University of Texas at Austin, Austin, Texas 78712, United States;* orcid.org/0000-0002-8737-451X; Email: milliron@che.utexas.edu

### Authors

**Sofia A. Shubert-Zuleta** − *Department of Chemistry, University of Texas at Austin, Austin, Texas 78712, United States;* orcid.org/0000-0003-0445-175X

**Bharat Tandon** − *McKetta Department of Chemical Engineering, University of Texas at Austin, Austin, Texas 78712, United States;* orcid.org/0000-0003-1108-9859

**Benjamin J. Roman** − *McKetta Department of Chemical Engineering, University of Texas at Austin, Austin, Texas 78712, United States;* orcid.org/0000-0003-2213-2533

**Xing Yee Gan** − *McKetta Department of Chemical Engineering, University of Texas at Austin, Austin, Texas 78712, United States;* orcid.org/0000-0001-5852-8463

Complete contact information is available at: https://pubs.acs.org/10.1021/acs.chemmater.2c03694


### Notes

The authors declare no competing financial interest.

## ■ ACKNOWLEDGMENTS

The authors acknowledge support from the National Science Foundation under award number CHE-1905263. S.S.Z. acknowledges the Graduate Research Fellowship Program under award number DGE-2137420. Support was also provided by the Center for Dynamics and Control of Materials: an NSF Materials Research Science and Engineering Center (NSF MRSEC) under Cooperative Agreement DMR-1720595.

## ■ REFERENCES


(1) Liu, X.; Swihart, M. T. Heavily-doped Colloidal Semiconductor and Metal Oxide Nanocrystals: An Emerging New Class of Plasmonic Nanomaterials. *Chem. Soc. Rev.* **2014**, *43*, 3908−3920.

(2) Faucheaux, J. A.; Stanton, A. L.; Jain, P. K. Plasmon Resonances of Semiconductor Nanocrystals: Physical Principles and New Opportunities. *J. Phys. Chem. Lett.* **2014**, *5*, 976−985.

(3) Comin, A.; Manna, L. New Materials for Tunable Plasmonic Colloidal Nanocrystals. *Chem. Soc. Rev.* **2014**, *43*, 3957−3975.

(4) Lounis, S. D.; Runnerstrom, E. L.; Llordés, A.; Milliron, D. J. Defect Chemistry and Plasmon Physics of Colloidal Metal Oxide Nanocrystals. *J. Phys. Chem. Lett.* **2014**, *5*, 1564−1574.

(5) Agrawal, A.; Cho, S. H.; Zandi, O.; Ghosh, S.; Johns, R. W.; Milliron, D. J. Localized Surface Plasmon Resonance in Semiconductor Nanocrystals. *Chem. Rev.* **2018**, *118*, 3121−3207.

(6) Tandon, B.; Ghosh, S.; Milliron, D. J. Dopant Selection Strategy for High-Quality Factor Localized Surface Plasmon Resonance from Doped Metal Oxide Nanocrystals. *Chem. Mater.* **2019**, *31*, 7752−7760.

(7) Runnerstrom, E. L.; Bergerud, A.; Agrawal, A.; Johns, R. W.; Dahlman, C. J.; Singh, A.; Selbach, S. M.; Milliron, D. J. Defect Engineering in Plasmonic Metal Oxide Nanocrystals. *Nano Lett.* **2016**, *16*, 3390−3398.

(8) Wainer, P.; Kendall, O.; Lamb, A.; Barrow, S. J.; Tricoli, A.; Gomez, D. E.; Van Embden, J.; Della Gaspera, E. Continuous Growth Synthesis of Zinc Oxide Nanocrystals with Tunable Size and Doping. *Chem. Mater.* **2019**, *31*, 9604−9613.

(9) Schimpf, A. M.; Ochsenbein, S. T.; Buonsanti, R.; Milliron, D. J.; Gamelin, D. R. Comparison of Extra Electrons in Colloidal n-type $Al^{3+}$-doped and Photochemically Reduced ZnO Nanocrystals. *Chem. Commun.* **2012**, *48*, 9352−9354.

(10) Diroll, B. T.; Gordon, T. R.; Gaulding, E. A.; Klein, D. R.; Paik, T.; Yun, H. J.; Goodwin, E. D.; Damodhar, D.; Kagan, C. R.; Murray, C. B. Synthesis of N-type Plasmonic Oxide Nanocrystals and the Optical and Electrical Characterization of Their Transparent Conducting Films. *Chem. Mater.* **2014**, *26*, 4579−4588.

(11) Ito, D.; Yokoyama, S.; Zaikova, T.; Masuko, K.; Hutchison, J. E. Synthesis of Ligand-Stabilized Metal Oxide Nanocrystals and Epitaxial Core/Shell Nanocrystals via a Lower-Temperature Esterification Process. *ACS Nano* **2014**, *8*, 64−75.

(12) Lounis, S. D.; Runnerstrom, E. L.; Bergerud, A.; Nordlund, D.; Milliron, D. J. Influence of Dopant Distribution on the Plasmonic Properties of Indium Tin Xxide nanocrystals. *J. Am. Chem. Soc.* **2014**, *136*, 7110−7116.

(13) Gibbs, S. L.; Dean, C.; Saad, J.; Tandon, B.; Staller, C. M.; Agrawal, A.; Milliron, D. J. Dual-Mode Infrared Absorption by Segregating Dopants within Plasmonic Semiconductor Nanocrystals. *Nano Lett.* **2020**, *20*, 7498−7505.

(14) Giannuzzi, R.; De Donato, F.; De Trizio, L.; Monteduro, A. G.; Maruccio, G.; Scarfiello, R.; Qualtieri, A.; Manna, L. Tunable Near-Infrared Localized Surface Plasmon Resonance of F, In-Codoped CdO Nanocrystals. *ACS Appl. Mater. Interfaces* **2019**, *11*, 39921−39929.

(15) Zandi, O.; Agrawal, A.; Shearer, A. B.; Reimnitz, L. C.; Dahlman, C. J.; Staller, C. M.; Milliron, D. J. Impacts of Surface Depletion on the Plasmonic Properties of Doped Semiconductor Nanocrystals. *Nat. Mater.* **2018**, *17*, 710−717.

(16) Agrawal, A.; Kriegel, I.; Runnerstrom, E. L.; Scotognella, F.; Llordes, A.; Milliron, D. J. Rationalizing the Impact of Surface Depletion on Electrochemical Modulation of Plasmon Resonance Absorption in Metal Oxide Nanocrystals. *ACS Photonics* **2018**, *5*, 2044−2050.
(17) Garcia, G.; Buonsanti, R.; Runnerstrom, E. L.; Mendelsberg, R. J.; Llordes, A.; Anders, A.; Richardson, T. J.; Milliron, D. J. Dynamically Modulating the Surface Plasmon Resonance of Doped Semiconductor Nanocrystals. *Nano Lett.* **2011**, *11*, 4415−4420.
(18) Ou, W.; Zou, Y.; Wang, K.; Gong, W.; Pei, R.; Chen, L.; Pan, Z.; Fu, D.; Huang, X.; Zhao, Y.; Lu, W.; Jiang, J. Active Manipulation of NIR Plasmonics: the Case of $Cu_{2-x}Se$ through Electrochemistry. *J. Phys. Chem. Lett.* **2018**, *9*, 274−280.
(19) Araujo, J. J.; Brozek, C. K.; Liu, H.; Merkulova, A.; Li, X.; Gamelin, D. R. Tunable Band-Edge Potentials and Charge Storage in Colloidal Tin-Doped Indium Oxide (ITO) Nanocrystals. *ACS Nano* **2021**, *15*, 14116−14124.
(20) Schimpf, A. M.; Lounis, S. D.; Runnerstrom, E. L.; Milliron, D. J.; Gamelin, D. R. Redox Chemistries and Plasmon Energies of Photodoped $In_2O_3$ and Sn-Doped $In_2O_3$ (ITO) Nanocrystals. *J. Am. Chem. Soc.* **2015**, *137*, 518−524.
(21) Ghini, M.; Curreli, N.; Lodi, M. B.; Petrini, N.; Wang, M.; Prato, M.; Fanti, A.; Manna, L.; Kriegel, I. Control of Electronic Band Profiles Through Depletion Layer Engineering in Core-Shell Nanocrystals. *Nat. Commun.* **2022**, *13*, 8773−8783.
(22) Schimpf, A. M.; Gunthardt, C. E.; Rinehart, J. D.; Mayer, J. M.; Gamelin, D. R. Controlling Carrier Densities in Photochemically Reduced Colloidal ZnO Nanocrystals: Size Dependence and Role of the Hole Quencher. *J. Am. Chem. Soc.* **2013**, *135*, 16569−16577.
(23) Engel, J. H.; Surendranath, Y.; Alivisatos, A. P. Controlled Chemical Doping of Semiconductor Nanocrystals Using Redox Buffers. *J. Am. Chem. Soc.* **2012**, *134*, 13200−13203.
(24) Jain, P. K.; Manthiram, K.; Engel, J. H.; White, S. L.; Faucheaux, J. A.; Alivisatos, A. P. Doped Nanocrystals as Plasmonic Probes of Redox Chemistry. *Angew. Chem.* **2013**, *125*, 13916−13920.
(25) Tandon, B.; Shubert-Zuleta, S. A.; Milliron, D. J. Investigating the Role of Surface Depletion in Governing Electron-Transfer Events in Colloidal Plasmonic Nanocrystals. *Chem. Mater.* **2022**, *34*, 777−788.
(26) Dorfs, D.; Härtling, T.; Miszta, K.; Bigall, N. C.; Kim, M. R.; Genovese, A.; Falqui, A.; Povia, M.; Manna, L. Reversible Tunability of the Near-Infrared Valence Band Plasmon Resonance in $Cu_{2-x}Se$ Nanocrystals. *J. Am. Chem. Soc.* **2011**, *133*, 11175−11180.
(27) Conti, C. R., III; McBride, J. R.; Strouse, G. F. Examining the Effect of Dopant Ionic Radius on Plasmonic M:ZnO Nanocrystals (M = $Al^{3+}$, $Ga^{3+}$, $In^{3+}$). *J. Phys. Chem. C* **2021**, *125*, 7772−7779.
(28) Conti, C. R., III; Quiroz-Delfi, G.; Schwarck, J. S.; Chen, B.; Strouse, G. F. Carrier Density, Effective Mass, and Nuclear Relaxation Pathways in Plasmonic Sn:$In_2O_3$ Nanocrystals. *J. Phys. Chem. C* **2020**, *124*, 28220−28229.
(29) Schimpf, A. M.; Thakkar, N.; Gunthardt, C. E.; Masiello, D. J.; Gamelin, D. R. Charge-Tunable Quantum Plasmons in Colloidal Semiconductor Nanocrystals. *ACS Nano* **2014**, *8*, 1065−1072.
(30) Lee, J. T.; Hati, S.; Fahey, M. M.; Zaleski, J. M.; Sardar, R. Surface-Ligand-Controlled Enhancement of Carrier Density in Plasmonic Tungsten Oxide Nanocrystals: Spectroscopic Observation of Trap-State Passivation via Multidentate Metal Phosphonate Bonding. *Chem. Mater.* **2022**, *34*, 3053−3066.
(31) Liu, Z.; Beaulac, R. Nature of the Infrared Transition of Colloidal Indium Nitride Nanocrystals: Nonparabolicity Effects on the Plasmonic Behavior of Doped Semiconductor Nanomaterials. *Chem. Mater.* **2017**, *29*, 7507−7514.
(32) Liu, Z.; Janes, L. M.; Saniepay, M.; Beaulac, R. Charge Storage and Quantum Confinement Resilience in Colloidal Indium Nitride Nanocrystals. *Chem. Mater.* **2018**, *30*, 5435−5443.
(33) Mendelsberg, R. J.; Garcia, G.; Li, H.; Manna, L.; Milliron, D. J. Understanding the Plasmon Resonance in Ensembles of Degenerately Doped Semiconductor Nanocrystals. *J. Phys. Chem. C* **2012**, *116*, 12226−12231.
(34) Gibbs, S. L.; Staller, C. M.; Milliron, D. J. Surface Depletion Layers in Plasmonic Metal Oxide Nanocrystals. *Acc. Chem. Res.* **2019**, *52*, 2516−2524.
(35) Gibbs, S. L.; Staller, C. M.; Agrawal, A.; Johns, R. W.; Saez Cabezas, C. A.; Milliron, D. J. Intrinsic Optical and Electronic Properties From Quantitative Analysis of Plasmonic Semiconductor Nanocrystal Ensemble Optical Extinction. *J. Phys. Chem. C* **2020**, *124*, 24351−24360.
(36) Graham, A. J.; Gibbs, S. L.; Saez Cabezas, C. A.; Wang, Y.; Green, A. M.; Milliron, D. J.; Keitz, B. K. *In Situ* Optical Quantification of Extracellular Electron Transfer Using Plasmonic Metal Oxide Nanocrystals. *ChemElectroChem.* **2022**, *9*, 27−49.
(37) Schrauben, J. N.; Hayoun, R.; Valdez, C. N.; Braten, M.; Fridley, L.; Mayer, J. M. Titanium and Zinc Oxide Nanoparticles Are Proton-Coupled Electron Transfer Agents. *Science* **2012**, *336*, 1298−1301.
(38) Valdez, C. N.; Schimpf, A. M.; Gamelin, D. R.; Mayer, J. M. Proton-Controlled Reduction of ZnO Nanocrystals: Effects of Molecular Reductants, Cations, and Thermodynamic Limitations. *J. Am. Chem. Soc.* **2016**, *138*, 1377−1385.
(39) Rinehart, J. D.; Schimpf, A. M.; Weaver, A. L.; Cohn, A. W.; Gamelin, D. R. Photochemical Electronic Doping of Colloidal CdSe Nanocrystals. *J. Am. Chem. Soc.* **2013**, *135*, 18782−18785.
(40) Jansons, A. W.; Hutchison, J. E. Continuous Growth of Metal Oxide Nanocrystals: Enhanced Control of Nanocrystal Size and Radial Dopant Distribution. *ACS Nano* **2016**, *10*, 6942−6951.
(41) Staller, C. M.; Gibbs, S. L.; Saez Cabezas, C. A.; Milliron, D. J. Quantitative Analysis of Extinction Coefficients of Tin-Doped Indium Oxide Nanocrystal Ensembles. *Nano Lett.* **2019**, *19*, 8149−8154.
(42) Nair, V.; Deepthi, A. Cerium(IV) Ammonium Nitrate - A Versatile Single-Electron Oxidant. *Chem. Rev.* **2007**, *107*, 1862−1891.
(43) Dong, A.; Ye, X.; Chen, J.; Kang, Y.; Gordon, T.; Kikkawa, J. M.; Murray, C. B. A Generalized Ligand-Exchange Strategy Enabling Sequential Surface Functionalization of Colloidal Nanocrystals. *J. Am. Chem. Soc.* **2011**, *133*, 998−1006.
(44) Saez Cabezas, C. A.; Ong, G. K.; Jadrich, R. B.; Lindquist, B. A.; Agrawal, A.; Truskett, T. M.; Milliron, D. J. Gelation of Plasmonic Metal oxide Nanocrystals by Polymer-Induced Depletion Attractions. *Proc. Natl. Acad. Sci. U. S. A.* **2018**, *115*, 8925−8930.
(45) Jarzebski, Z. M. Preparation and Physical Properties of Transparent Conducting Oxide Films. *Phys. Stat. Sol.* **1982**, *71*, 13−41.
(46) Petrini, N.; Ghini, M.; Curreli, N.; Kriegel, I. Optical Modeling of Plasmonic Nanoparticles with Electronically Depleted Layers. *J. Phys. Chem. C* **2023**, *127*, 1576−1587.
(47) Yin, P.; Tan, Y.; Ward, M. J.; Hegde, M.; Radovanovic, P. V. Effect of Dopant Activation and Plasmon Damping on Carrier Polarization in $In_2O_3$ Nanocrystals. *J. Phys. Chem. C* **2019**, *123*, 29829−29837.
(48) Fang, H.; Hegde, M.; Yin, P.; Radovanovic, P. V. Tuning Plasmon Resonance of $In_2O_3$ Nanocrystals throughout the Mid-Infrared Region by Competition between Electron Activation and Trapping. *Chem. Mater.* **2017**, *29*, 4970−4979.
(49) Carroll, G. M.; Schimpf, A. M.; Tsui, E. Y.; Gamelin, D. R. Redox Potentials of Colloidal n-Type ZnO Nanocrystals: Effects of Confinement, Electron Density, and Fermi-Level Pinning by Aldehyde Hydrogenation. *J. Am. Chem. Soc.* **2015**, *137*, 11163−11169.
(50) Schimpf, A. M.; Knowles, K. E.; Carroll, G. M.; Gamelin, D. R. Electronic Doping and Redox-Potential Tuning in Colloidal Semiconductor Nanocrystals. *Acc. Chem. Res.* **2015**, *48*, 1929−1937.
(51) Brookhart, M.; Grant, B.; Volpe, A., Jr. $[(3,5\text{-}(CF_3)_2C_6H_3)_4B]$-$[H(OEt_2)_2]^+$: A Convenient Reagent for Generation and Stabilization of Cationic, Highly Electrophilic Organometallic Complexes. *Organometallics* **1992**, *11*, 3920−3922.
(52) Le Bras, J.; Jiao, H.; Meyer, W. E.; Hampel, F.; Gladysz, J. A. Synthesis, Crystal Structure, and Reactions of the 17-valence-electron Rhenium Methyl Complex $[(\eta_5\text{-}C_5Me_5)Re(NO)(P(4\text{-}C_6H_4CH_3)_3)$-$(CH_3)]\bullet^+B(3,5\text{-}C_6H_3(CF_3)_2)_4^-$: Experimental and Computational


https://doi.org/10.1021/acs.chemmater.2c03694
Chem. Mater. 2023, 35, 3880−3891

Bonding Comparisons with 18-electron Methyl and Methylidene Complexes. *J. Organomet. Chem.* **2000**, *616*, 54−66.
(53) Hamberg, I.; Granqvist, C. G. Evaporated Sn-doped $In_2O_3$ Films: Basic Optical Properties and Applications to Energy-Efficient Windows. *J. Appl. Phys.* **1986**, *60*, R123−R159.





https://doi.org/10.1021/acs.chemmater.2c03694
*Chem. Mater.* 2023, 35, 3880−3891